

Suppression of magnetic phase transition at high magnetic field and non-Debye's nature of nano-crystalline $\text{Gd}_2\text{CoMnO}_6$: a detail study of physical properties

Ilyas Noor Bhatti^a Imtiaz Noor Bhatti^b Rabindra Nath Mahato^c and M. A. H. Ahsan^a

^aDepartment of Physics, Jamia Millia Islamia University, New Delhi - 110025, India;

^bDepartment of School Education, Government of Jammu and Kashmir, India;

^cSchool of Physical Sciences, Jawaharlal Nehru University, New Delhi - 110067, India;

ARTICLE HISTORY

Compiled January 5, 2022

ABSTRACT

Structural, magnetization, phonon behavior, and dielectric response of nano-crystalline $\text{Gd}_2\text{CoMnO}_6$ have been presented in this paper. The study shows that the material crystallizes in $P2_1/n$ phase group of monoclinic crystal structure. XPS measurement shows Co^{2+} and Mn^{4+} oxidation states are present in the sample. Magnetization study reveals that sample undergoes a ferromagnetic ordering of Co^{2+} and Mn^{4+} magnetic ions around $T_c \sim 132$ K. However we have seen that with the application of external magnetic field the phase transition is largely suppressed. Raman study reveals the presence spin-phonon coupling in $\text{Gd}_2\text{CoMnO}_6$. Dielectric study reveals that the sample shows large dielectric constant and strong dispersion in mid frequency range. The dielectric loss shows there are two relaxation processes present in the material with different relaxation time and which are driven by thermally activated relaxation mechanics. Further, the Nyquist plot and AC conductivity study shows that this sample is non-Debye's in nature.

KEYWORDS

Oxides, Nano-crystalline, Magnetism, Raman spectroscopy, Dielectric, Nyquist plot

1. Introduction

Multiferroicity, magnetoelectric, magnetocapacitance and magnetocaloric properties are seen in rare-earth based double perovskite manganites R_2BMnO_6 (R = rare-earth and B = Ni/Co) received great attention of researchers due to the potential for device applications.[1–7] The superexchange dominated magnetic ordering of $(\text{Co}/\text{Ni})^{2+}$ and Mn^{4+} spins give ferromagnetic nature to these compounds where the magnetic phase transition depends on the rear-earth ion which cause structural distortion in double perovskite structure. However the B-site disorder in double perovskite with $(\text{Co}/\text{Ni})^{3+}$ and $\text{Mn}^{3+}/\text{B}^{2+}$ - B^{2+} result in antiferromagnetic ordering at lower temperature.[8] It is a known fact that the transition temperature T_c of ordered Co/Ni -Mn sublattice decreases with reducing radii of rare-earth cations.[9, 10] Apart from this the R (rare earth) ions have the spin moment which shows magnetic interaction via R - R ions and

align antiferromagnetic with B/Mn sublattice at low temperatures.[11, 12] These compounds have potential to show magnetic field controllable polarization/ capacitance.

There have been several reports on bulk polycrystalline as well as single crystal rare-earth based manganite double perovskite compounds to understand various physical properties. The Ni/Mn based double perovskite has been studied more as compared to Co/Mn. However, there have been several exotic properties have been seen in $R_2\text{CoMnO}_6$ compounds as well. For instance, recently $\text{La}_2\text{CoMnO}_6$ a ferromagnetic material with $T_c \sim 225$ K [13], it is found that material shows spin-phonon coupling in thin-films where both ordered and disordered sample have been investigated.[14] $\text{Pr}_2\text{CoMnO}_6$ is another member of this series which shows a ferromagnetic ordering and feature Griffith's phase in the paramagnetic state close to phase transition.[15–17] Various other compounds have been studied and found interesting properties like multiferroicity in $(\text{Lu/Y})_2\text{CoMnO}_6$,[18, 19] metamagnetic transition in $(\text{Eu/Tb})_2\text{CoMnO}_6$,[20, 21] and pyroelectricity and magnetocapacitance in $\text{Lu}_2\text{CoMnO}_6$ [22]. Among these double perovskites $\text{Gd}_2\text{CoMnO}_6$ have been studied to understand its physical properties whereas most of the efforts have been made to investigate the giant magnetocaloric effect [23] at low temperature. Further spin-glass frozen state [24] and metamagnetic transition[25] have also been reported for polycrystalline $\text{Gd}_2\text{CoMnO}_6$ close to ferromagnetic transition. Here, our focus is to investigate the detail physical properties of nano-crystalline $\text{Gd}_2\text{CoMnO}_6$. We focus our study to understand the effect of the magnetic field on the magnetic phase transition since earlier literature gives evidence of metamagnetic transition and spin-glass state in this material. Further, low temperature antiferromagnetic ordered Gd^{3+} ions corresponding to Co/Mn sublattice may be effected at the high magnetic field. Dielectric response in rear-earth based manganites are interesting and we will also focus on this study in this paper.

In this paper, we have investigated nano-crystalline $\text{Gd}_2\text{CoMnO}_6$ using magnetization, Raman spectroscopy and dielectric measurements. The sol-gel prepared nano-crystalline $\text{Gd}_2\text{CoMnO}_6$ is characterized by X-ray diffraction for structural study. The sample is found to be single phase and crystallize in $P2_1/n$ space group of the monoclinic crystal structure. Magnetization study reveals that the material shows ferromagnetic transition around 130 K and a low temperature antiferromagnetic ordering of Gd sublattice. The magnetic field greatly influences the magnetic structure of $\text{Gd}_2\text{CoMnO}_6$. Raman study shows strong spin-phonon coupling in this material. The dielectric response shows large frequency dispersion, dielectric relaxation is seen in the tangent loss. Impedance spectroscopy shows the material deviates from ideal Debye's model. AC conductivity shows the quantum mechanical tunneling conduction mechanism in this material.

2. Experimental details

Nano-crystalline sample of double perovskite $\text{Gd}_2\text{CoMnO}_6$ was prepared by sol-gel method. Stoichiometric amounts of $\text{Gd}(\text{NO}_3)_3 \cdot 6\text{H}_2\text{O}$ and $\text{Co}(\text{NO}_3)_2 \cdot 6\text{H}_2\text{O}$ and $\text{C}_4\text{H}_6\text{MnO}_4 \cdot 4\text{H}_2\text{O}$ dissolves in doubled distilled water separate beakers. Citric acid is taken in 3:1 ration and dissolved in distilled water. All these solutions are placed on a stirrer for sufficient time to obtain a clear solution. After this, the solutions are mixed in large beaker which is filled up to 400 ml with distilled water. The mixture of solutions was then placed on a magnetic stirrer for 24 hours at 90 °C. After evaporation of water, the solution turned in to gel form which is then heated at 300 °C to

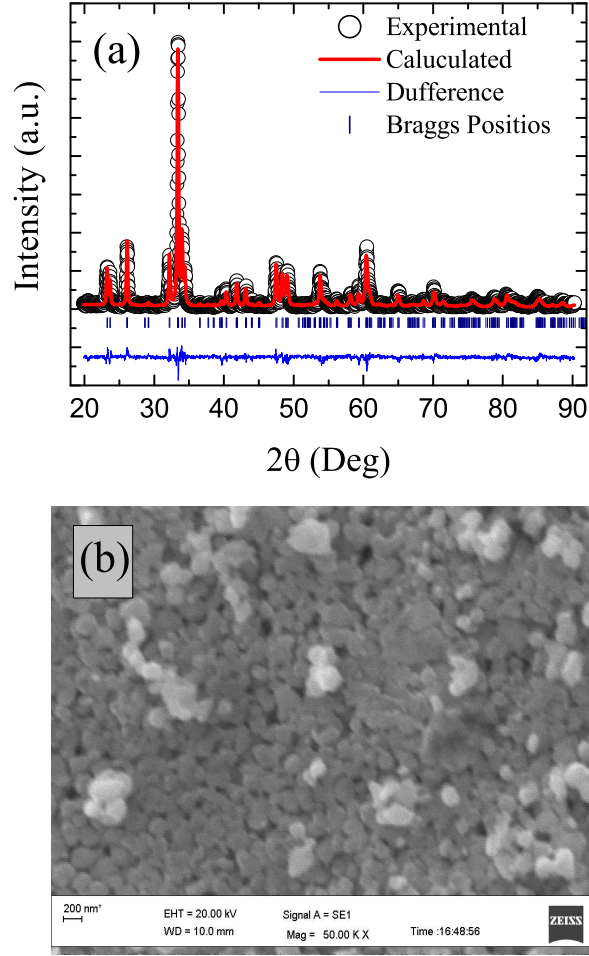


Figure 1. (Color online) (a) Rietveld refinement of powder XRD data for nano-crystalline $\text{Gd}_2\text{CoMnO}_6$ (b) SEM micrograph for partial size calculation.

obtain solid foam. This foam then collected from the beaker and ground in mortar and pestle to crush it into powder form. The powder sample is then sintered at 850 °C for 12 hours. Similar method has been adopted for other material [16, 26, 27]. The sample was then characterized by X-ray diffraction (XRD) ($\text{Cu}_{K\alpha}$, $\lambda = 1.5406 \text{ \AA}$) for structural study. The XRD data is collected in the 2θ range of 20-90° with a step size of 0.02°. The XPS measurements were performed with base pressure in the range of 10^{-10} mbar using a commercial electron energy analyzer (Omicron nanotechnology) and a non-monochromatic $\text{Al}_{K\alpha}$ X-ray source ($h\nu = 1486.6 \text{ eV}$). The XPSpeakfit software has been used to analyze the XPS data. The magnetic measurements have been carried out on the Physical properties measurement system (PPMS) by Cryogen Inc. Temperature dependent Raman spectra have been collected using Diode based laser (with output wavelength $\lambda = 473 \text{ nm}$, coupled with a Labram-HR800 micro-Raman spectrometer. Dielectric measurements in the frequency range from 1 Hz to 5.5 MHz were performed using a computer controlled dielectric setup mounted on CCR with operating temperature range of 15 to 320 K. The dielectric parameters were measured using LCR meter.

3. Result and Discussions

3.1. Structural study

XRD was done at room temperature for the structural study of the sample. Rietveld refinement was performed with Fullprof program for the analysis of crystal structure. Fig. 1(a) represents the XRD pattern and Rietveld refinement of the $\text{Gd}_2\text{CoMnO}_6$ sample. Fig. represents black circle for experimental data, red solid line for calculated data, blue lines for difference and navy blue bars represent Braggs positions. The Rietveld refinement shows that the XRD pattern is well fitted with the calculated one which confirms the phase purity of the sample. The goodness of fit χ^2 and R_{wp}/R_{exp} ratio as 1.67 and 1.2487 respectively are acceptable and in agreement with literature.[27–30] The crystal structure of $\text{Gd}_2\text{CoMnO}_6$ is monoclinic with space group is $P2_1/n$. The lattice parameters obtained from structural analysis a , b and c are 5.2755 Å, 5.5616 Å and 7.5212 Å respectively. The angle $\beta = 90.0747^\circ$ and unit cell volume is 220.6736 Å³. Further, to obtain the particle size of the $\text{Gd}_2\text{CoMnO}_6$ sample we have done the scanning electron microscopy. Fig. 1(b) shows the SEM image obtained for the nanocrystalline structure having a uniform distribution of nano-particles. The SEM image is analyzed with ImageJ software. The detail analysis of SEM image shows the average crystalline size for the present compound is ~ 110.9 nm.

3.2. X-ray photoelectron spectroscopy (XPS)

Charge state of cations present in a material decides the electronic and magnetic ground state of that material. Charge state of cations can be understood by XPS measurement on a material here we have recorded the core level spectra of Co, Mn and Gd in $\text{Gd}_2\text{CoMnO}_6$ sample. The XPS spectra of these elements are fitted with XPS PEAKFIT 4.1.

Fig. 2a shows the core level spectrum of Co $2p_{3/2}$ at 796.01 eV corresponding to +2 charge state which is in agreement with reported literature.[31–35] Besides the strong Co $2p$ peak a small less intense satellite peak is also been observed close to Co $2p$ peaks(see figure).

Fig. 2b shows the Mn $2p$ core level spectrum along with peak fitting. Here, Mn $2p_{3/2}$ peaks of core level is presented which is located at 642 eV, which confirms the +4 oxidation state of Mn cations. A relatively small intensity satellite peak is also been seen at higher energy side of Mn $2p_{3/2}$ peak.[27, 34–38]

Fig. 2c shows that the Gd $4d$ core level spectra, which split into two spin-orbital split peaks Gd $4d_{5/2}$ and Gd $4d_{3/2}$ are located at 142.6 and 148.03 eV respectively (see figure). These peak positions are consistent with literature and corresponds to +3 oxidation state of Gd cations.[39, 40] XPS study shows that the oxidation states of Co, Mn and Gd cations present in $\text{Gd}_2\text{CoMnO}_6$ are +2, +4 and +3 respectively, which is in agreement with the structural results since with Mn^{+4} and Co^{+2} an ordered structure is expected for Mn-Co double perovskite structure.

3.3. DC Magnetization study

Temperature dependent DC magnetization $M(T)$ have been measured for $\text{Gd}_2\text{CoMnO}_6$ in both the zero field cooled (ZFC) and field cooled (FC) protocol. Fig. 3a shows the $M(T)$ data measured in the temperature range from 2 K to 300 K while warming the sample from low temperature. The M_{ZFC} data is collected in H

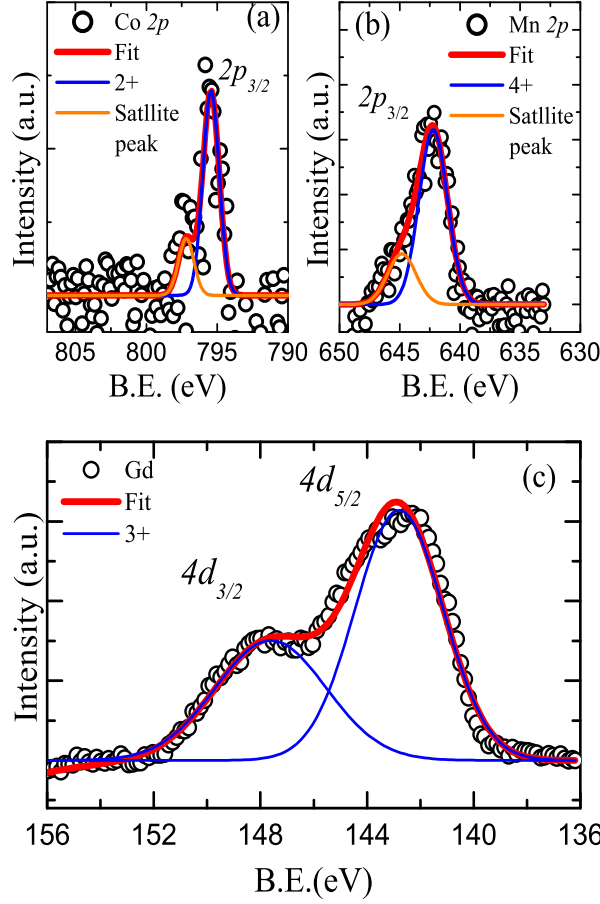


Figure 2. (Color online) Figure presents the XPS spectra of (a) Co 2p (b) Mn 2p (c) Gd 4d core levels, where Open circles are experimental data, the red solid lines are the overall fitting and the colored solid lines are the fitted peaks (see figure).

= 100 Oe applied magnetic field (H). Whereas M_{FC} is measured at various fields viz, 100 Oe, 250 Oe, 500 Oe and 1000 Oe shown in Fig. 3a. We observe that the M_{ZFC} and M_{FC} remain almost constant with decreasing temperature from 300 K to ~ 140 K and both M_{ZFC} and M_{FC} curves overlap on each other. However, with further decrease temperature the dc magnetization M began to increase sharply. For clarity M_{ZFC} is shown in the inset of Fig. 3a, it is evident that the M_{ZFC} shows a sharp increase in the magnetic moment below 140 K and shows a peak around 130 K whereas with further lowering temperature the moment starts decreasing and attains a stable constant value and forms a plateau. However, at a very low temperature below 40 K, a downfall in M_{ZFC} is observed (see inset Fig. 3a). It is evident from Fig. 3a that the M_{FC} data continuously increases with the decreasing temperature below 140 K. However with further decreasing temperature the M_{FC} data shows a broad peak centered around 50 K and the M_{FC} suffer a downfall in magnetic moment below this temperature down to lowest measurable temperature 2 K. The sharp increase in $M(T)$ data below 140 K is signature of magnetic phase transition from random spin paramagnetic (PM) to ordered ferromagnetic (FM) phase. We observed a large bifurcation between M_{ZFC} and M_{FC} below 130 K. To better understand the nature of this magnetic phase transition in $\text{Gd}_2\text{CoMnO}_6$ we have measured M_{FC} at various applied magnetic fields (See Fig

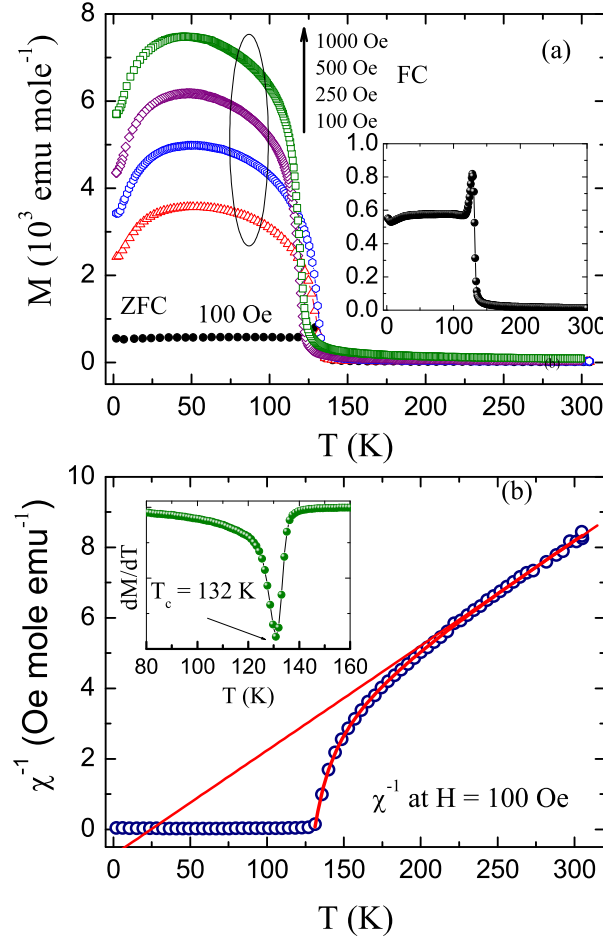


Figure 3. (Color online) (a) Temperature dependent magnetization data $M(T)$ shown for $\text{Gd}_2\text{CoMnO}_6$ measured at different low fields. (b) $M(T)$ data plotted in terms of inverse susceptibility χ^{-1} , solid line is fitting due to Curie Weiss Law. Inset shows dM/dT vs T plot showing T_c for $\text{Gd}_2\text{CoMnO}_6$.

3a). We observe that with increasing H the magnetization increases which is expected because more and more spins will orient themselves in the field direction. Further, in the M_{FC} data at the different applied field we observed that with increasing field T_c shifts to the higher temperature. The PM-FM phase transition in $\text{Gd}_2\text{CoMnO}_6$ appears with a sharp increase in magnetization due to cooperative spin interaction. dM/dT vs T plot is often used to estimate the transition temperature T_c , the minima i.e. point of inflection in this plot gives T_c . Inset of Fig. 3b the shown dM/dT vs T plotted from M_{FC} taken at 100 Oe, it is evident from the figure that T_c for $\text{Gd}_2\text{CoMnO}_6$ is 132 K.

It is evident from the static magnetization data that in $\text{Gd}_2\text{CoMnO}_6$ shows ferromagnetic ordering below 132 K. To understand the magnetic behavior of $\text{Gd}_2\text{CoMnO}_6$ we consider the high spin state for Mn/Co cations. In the above section, we have seen our XPS result confirms that the Mn and Co cations are in +4 and +2 oxidation states respectively. In high spin state the Mn^{4+} ($t_{2g}^3 \uparrow \uparrow \uparrow e_g^0 -$) gives $S = 3/2$ and Co^{2+} ($t_{2g}^5 \uparrow \downarrow \uparrow \downarrow \uparrow e_g^2 \uparrow \uparrow$) yield $S = 3/2$ with spin only formula. These cations engage in superexchange interaction below 132 K via $\text{Co}^{2+}\text{-O-Mn}^{4+}$ network and give rise to a ferromagnetic state in $\text{Gd}_2\text{CoMnO}_6$. However, the Gd^{3+} $[\text{Xe}](4f^7)$ with $S =$

7/2 present in the material is also magnetic. It is believed that the rare-earth spins become interactive only at low temperatures. The magnetization data (see Fig. 3a) shows a broad peak at 50 K and shows a downfall at low temperature, perhaps it is the anti-ferromagnetic character. In this temperature range the Gd^{3+} spins experience exchange interaction via oxygen as $\text{Gd}^{3+}\text{-O}^{2+}\text{-Gd}^{3+}$ and develops an ordered state of Gd sublattice. It is worth to mention that in the temperature dependent magnetization data that the anti-ferromagnetic ordering is observed at low temperature. The antiferromagnetic ordering is attributed because the ordered Gd sublattice is aligned in the opposite direction of the Mn/Co sublattice.

Fig. 3b shows the temperature dependent inverse magnetic susceptibility i.e. χ^{-1} vs T plotted using M_{FC} data from Fig. 3a at 100 Oe. It is evident from the general feature of the χ^{-1} plot that above T_c inverse susceptibility shows deviation from conventional Curie Weiss law. It is worth to mention here that for double perovskite compounds such deviation is expected. It is believed that the rare earth (Gd^{3+}) sublattice remains non-interactive at high temperature in the network of Co/Mn lattice. Thus a modified Curie Weiss law described as below is used to understand the magnetic behavior in $\text{Gd}_2\text{CoMnO}_6$: [41, 42]

$$\chi = \frac{C_{TM}}{T - \theta_{TM}} + \frac{C_{Gd}}{T - \theta_{Gd}} \quad (1)$$

Here C_{TM} and θ_{TM} is Curie Constant and paramagnetic Curie temperature for transition metal sublattice. Whereas C_{RE} and θ_{RE} are the Curie Constant and paramagnetic Curie temperatures for rare earth sublattice. We have performed the non-linear fitting of susceptibility data measured at 100 Oe for $\text{Gd}_2\text{CoMnO}_6$ shown in Fig. 3b. The fitting is done above T_c in the temperature range 80 K to 300 K. The fitting parameters obtained from fitting of χ^{-1} with Eq. 1 gives the value of C_{TM} and θ_{TM} as 3.151(6) emu K mole $^{-1}$ Oe $^{-1}$ and 131 K respectively. The effective paramagnetic moment (μ_{eff}^{TM}) is calculated using these fitting parameters come out to be 5.250(2) $\mu_B/f.u.$, the obtained values are in close to theoretical calculations. The value of C_{RE} and θ_{RE} for Gd sublattice for agreement $\text{Gd}_2\text{CoMnO}_6$ are 32.26 emu K mole $^{-1}$ Oe $^{-1}$ and -18.51(2) K respectively. The negative value of θ_{RE} signifies that the Gd^{3+} spins are anti-ferromagnetic ordering relative to Mn/Co sublattice. The modified Curie Weiss law in Eq. 1 is presented considering non-interacting Mn/Co and Gd sublattice in this compound.

For further understanding of the low temperature downfall in magnetization data and magnetic transition, we have measured the $M(T)$ at different fields as stated above (see Fig. 3a). It is observed that there is an evolution in the general feature of the $M(T)$ curve. Thus it is quite evident from the magnetization data that the spin structure is greatly influenced at the higher magnetic field. In Fig. 4a we have shown the magnetization data collected at 10 kOe applied field. It is observed that the magnetization data M_{ZFC} and M_{FC} curves show a similar kind of magnetic transition around 130 K. However, below T_c the feature of magnetic data changes greatly as compared to low field data presented in Fig. 3a. Below T_c there is clear bifurcation between the M_{ZFC} and M_{FC} branches. M_{ZFC} decrease with decreasing temperature attains a dip around 30 K and then shown a sharp upturn and increases monotonically till lowest measured temperature. On the other hand the M_{FC} increases with decreasing temperature. This feature in $M(T)$ data measured at the high field of 10 kOe is unlike observed at the low field where both the M_{ZFC} and M_{FC} show an anti-ferromagnetic ordered state.

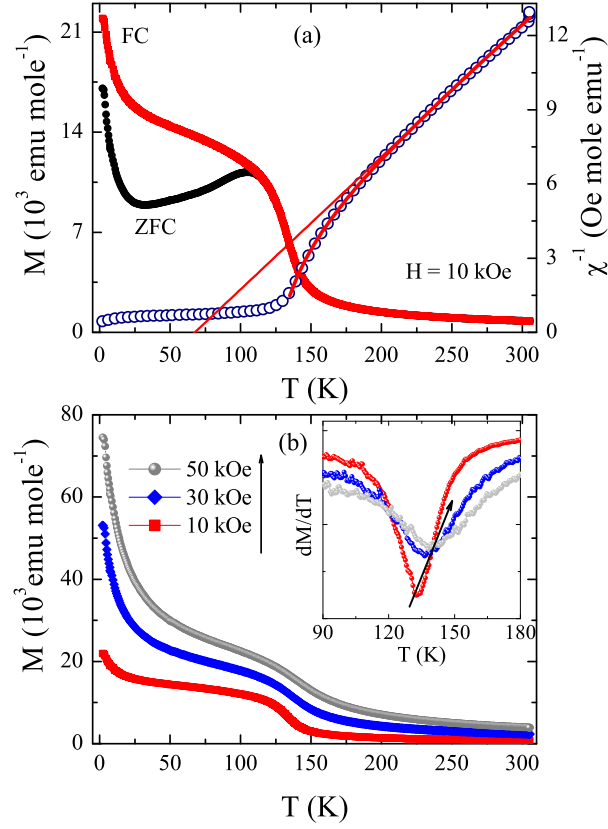


Figure 4. (Color online) (a) Temperature dependent magnetization data $M(T)$ shown for $\text{Gd}_2\text{CoMnO}_6$ measured at high fields 10 kOe (left axis), $M(T)$ data plotted in terms of inverse susceptibility χ^{-1} , solid line is fitting due to Curie Weiss Law (right axis). (b) Field Cooled (FC) magnetization data collected at different fields are shown for $\text{Gd}_2\text{CoMnO}_6$. Inset shows dM/dT vs T plot showing c for $\text{Gd}_2\text{CoMnO}_6$.

To further deepen our understanding we have measured M_{FC} at the even higher field and presented in Fig. 3b it is quite evident that the low temperature downfall in M_{FC} vanishes. Further, the magnetic transition at 130 K seems to get smoother at high field. Such behavior of spins at the higher field needs to be investigated using some advanced techniques. However, it seems that the spins at the higher field are becoming non-cooperative and result in weakening of magnetic ordering. To further understand this magnetic nature in $\text{Gd}_2\text{CoMnO}_6$ we have plotted the magnetization data in terms of magnetic susceptibility. It is observed that the diversion in χ^{-1} above T_c decreases which is quite large at low field. The general feature of $M(T)$ curve is largely affected by the increasing magnetic field.

Isothermal magnetization $M(H)$ data measured in both the ferromagnetic state at 110 K and antiferromagnetic state at 2 K up to ± 50 kOe applied magnetic field as shown in Fig. 5a and 5b. $M(H)$ curve shows in Fig. 5a shows no hysteresis and the $M(H)$ curve shows a typical anti-ferromagnetic type features. Further, Arrott plot (M^2 vs H/M) shown in Fig. 5b gives the negative intercept which indicates there is no spontaneous magnetization present in this material at 2 K. However, the $M(H)$ data shown in Fig. 5c is collected in the ferromagnetic ordered state at 110 K seems quite interesting. The hysteresis present in the $M(H)$ curve confirms the ferromagnetic ordering at this temperature. The $M(H)$ data do not saturate even at the highest applied field. The magnetic moment at the highest applied field of 50 kOe is about

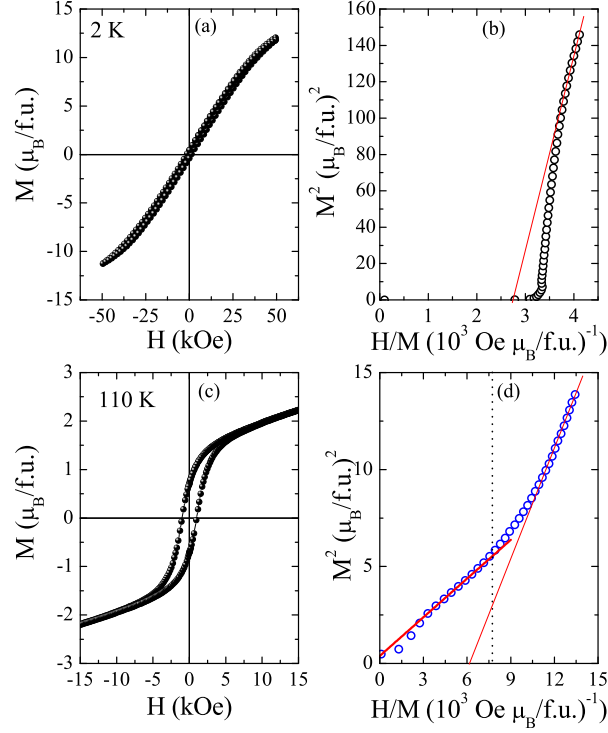


Figure 5. (Color online) (a, c) Isothermal data collected at 2 K and 110 K in the applied field of ± 50 kOe. (b, d) Virgin curves of $M(H)$ (a, c) is plotted in terms of Arrott plot M^2 vs H/M .

$3.7 (\mu_B/\text{f.u.})$. Whereas the remanent magnetization M_r and coercive force H_c is $0.7 \mu_B/\text{f.u.}$ and 1000 Oe respectively. In Fig. 5d Arrott plot is shown for $M(H)$ data collected at 110 K exhibits some interesting feature. We observe two slopes from the Arrott plot marked two regions, below 15 kOe the extrapolation cut the positive M^2 axis and gives a spontaneous magnetic moment $\mu_s = 0.6228 \mu_B/\text{f.u.}$ However, above this field, a steep increase is observed which when extrapolated intercepts the negative M^2 axis which signifies no ferromagnetic ordering present. Thus our results reveals that the magnetic behavior changes with at higher field seen in $M(T)$ is may be due to the non-cooperative behavior of spins at the higher magnetic field in $\text{Gd}_2\text{CoMnO}_6$. We believe that detail local probing and high field investigation is needed to understand this scenario in depth.

3.4. Temperature dependent Raman study

Raman spectra have been recorded at different temperatures across magnetic phase transition in the temperature range of 300 K to 10 K $\text{Gd}_2\text{CoMnO}_6$. In Fig. 6a Raman spectra have been shown at selective temperatures for clarity the data each curve is shifted upward. Raman data shows the presence of multiple phonon are active in $\text{Gd}_2\text{CoMnO}_6$ double perovskite material. However, our main focus is on the strongest mode present at 641 cm^{-1} known as breathing mode, since $\text{Gd}_2\text{CoMnO}_6$ crystalizes in $P2_1/n$ space group thus this breathing mode obeys A_{1g} symmetry. All these modes present in the Raman spectra of $\text{Gd}_2\text{CoMnO}_6$ are believed to be linked with stretching/bending and rotation of $(\text{Co/Mn})\text{O}_6$ octahedra. Symmetric stretching of the $(\text{Co/Mn})\text{O}_6$ octahedra gives a strong mode at 636 cm^{-1} and mode at 496 cm^{-1}

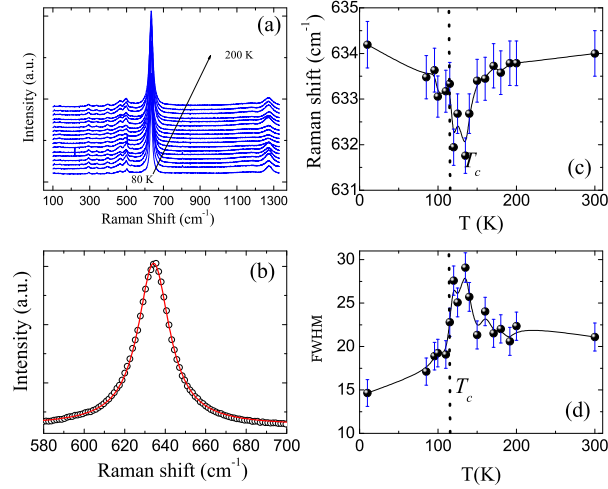


Figure 6. (Color online) (a) Raman spectra of Gd₂CoMnO₆ at selective temperatures. (b) shows the A_{1g} Raman mode at 641 cm⁻¹ solid line is the Lorentzian fit. Temperature Variation of (c) Raman shift (d) FWHM for Raman mode at 641 cm⁻¹.

is due to antisymmetric stretching and bending.[43] A weak modes at ~ 1278 cm⁻¹ called second-order overtones of the breathing mode.[44] Raman spectra show a little modification in both the intensity and peak positions of each mode with temperature variation.

To further understand the evolution of Raman spectra with temperature, we have fitted the spectrum collected at different temperatures with the Lorentzian function. Fig. 6b shows the line shape along with Lorentz fitting of A_{1g} mode at 150 K. From the fitting of Raman spectra we obtained the peak position of Raman mode and line width. The temperature variation of peak position and line width is shown in Fig. 6c and 6d respectively. It is evident, both the position and line width show a deviation from anharmonic behavior around the magnetic ordering temperature T_c 132 K (see magnetization section). The deviation at T_c is known due to the extra scattering mechanism involved due to spin-lattice interaction present in the material. Such deviations in mode frequency shift and line narrowing have been reported for many such systems in earlier literature.

3.5. Dielectric study

Dielectric properties of a material are defined in terms of the complex relative permittivity (ϵ), which consists of two components namely a real and an imaginary component. The real part of the complex permittivity is known as the dielectric constant, which defines the measure of energy stored in material from external electric field in which it is placed. The imaginary part is known as the loss factor. The lag between the change in polarization and the applied electric field makes the permittivity a complex entity given as:[45–49]

$$\epsilon = \epsilon' + i\epsilon'' \quad (2)$$

where, ϵ' ϵ'' is the real part and the imaginary part of the permittivity respectively. The ratio of imaginary part of permittivity to the real part of permittivity is given by

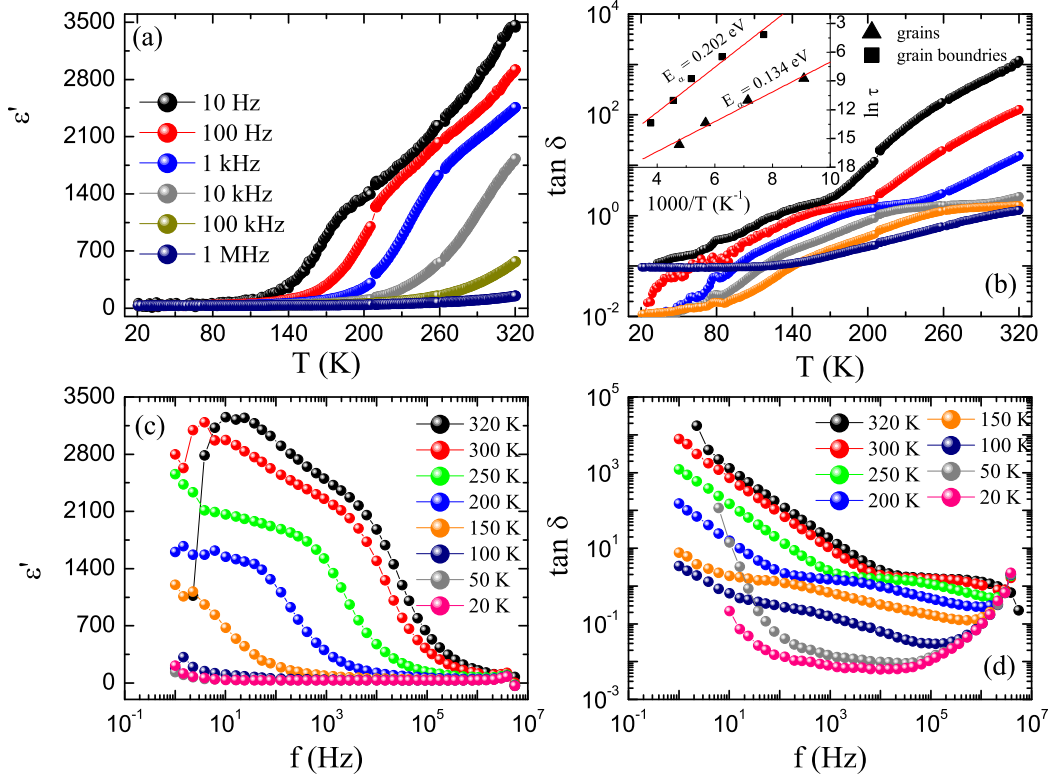


Figure 7. (Color online) Temperature dependent (a) dielectric constant (ϵ') (b) loss tangent ($\tan \delta$) measure for $\text{Gd}_2\text{CoMnO}_6$. Inset of Fig. (b) plot of relaxation time vs normalized temperature obtained from tangent loss data in Fig. 7(b). Frequency dependent (c) dielectric constant (ϵ') (d) loss tangent ($\tan \delta$) measured at selective temperatures (see figure) in the frequency range 1 Hz to 5.5 MHz.

following relation and called dielectric loss factor:[45, 46]

$$\tan \delta = \frac{\epsilon''}{\epsilon'} \quad (3)$$

Dielectric constant (ϵ') and loss ($\tan \delta$) were measured between 20 K and 300 K temperature at different frequencies for $\text{Gd}_2\text{CoMnO}_6$. Fig. 7a and 7b represent the ϵ' and $\tan \delta$ as a function of temperature. Further, the material showing relaxor behavior with various relaxation mechanisms give rise to a plateau in $\epsilon'(T)$ and respond with peaks in $\tan \delta$. For nano-crystalline $\text{Gd}_2\text{CoMnO}_6$ we have observed that at low temperature the ϵ' at all frequencies is merged. However, with increasing temperature, the ϵ' started increasing sharply around 140 K and with further increases in temperature the ϵ' shows strong dispersion with frequency. Further, with increasing frequencies, ϵ' decreases more rapidly. The charge accumulation at the grain boundaries attributes to the higher value of ϵ' at low frequency. By carefully looking into the tangent loss curve $\tan \delta$ in Fig. 7b it is found that there are two broad humps at low temperature. Such kind of peak in $\tan \delta$ curve is a characteristics of the relaxor phenomenon. With increasing frequency the observed peaks shift towards higher temperature. It is believed that the relaxation mechanism at low temperature is due to grains whereas the one on the higher temperature side is due to grain boundaries.

The relaxation mechanism and its origin can be analyzed by the Arrhenius law

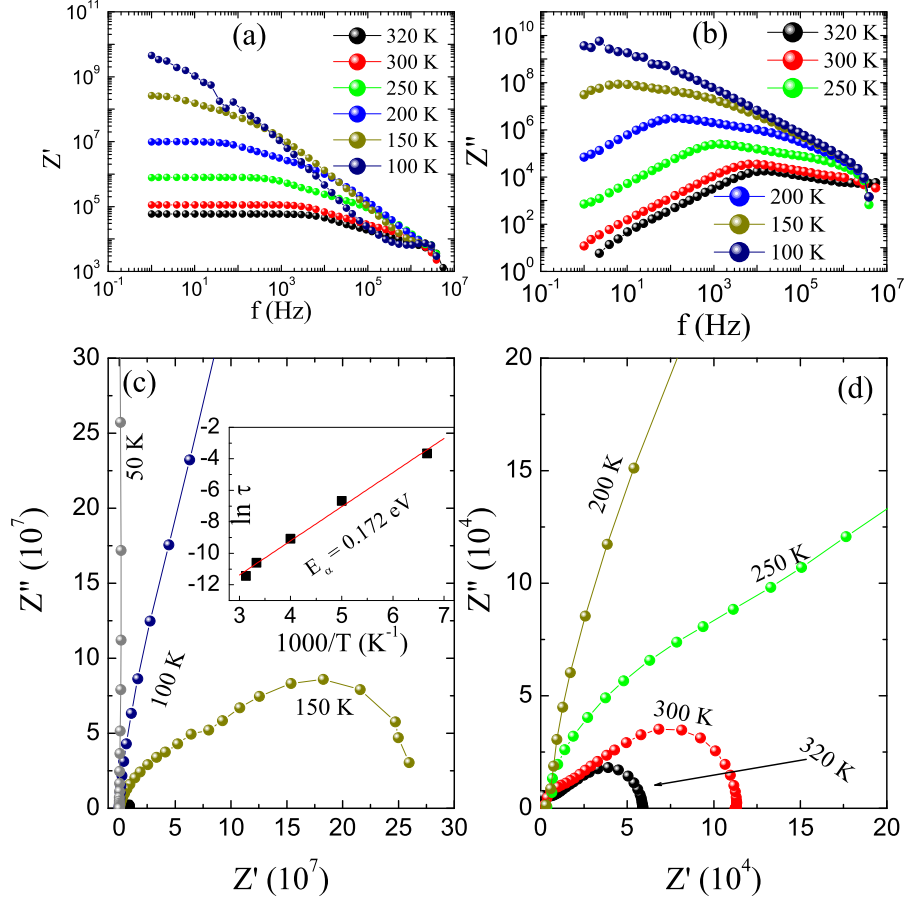


Figure 8. (Color online) Frequency dependent data (a) real part of impedance (Z') (b) imaginary part of impedance (Z'') collected at selective temperatures. Inset of Fig (c) shows the variation of relaxation time vs normalized temperature obtained from Fig. 8b. (c), (d) Niquest plot Z' vs Z'' for $\text{Gd}_2\text{CoMnO}_6$.

given by, $\tau_{\tan\delta} = \tau_0 \exp(-E_a/k_B T)$ where, T is the temperature corresponding to the peak observed in the $\tan\delta$ curve at a particular frequency $f_{\tan\delta}$, f_0 is characteristic frequency, E_a is the activation energy of the relaxation process and k_B is the Boltzmann constant. The value of τ can be obtained from frequency $f_{\tan\delta}$ by the relation $\tau = 1/2\pi f$. Inset of Fig. 7b shows the plot of τ vs $1000/T$ for both the relaxation peaks. The data shown in the inset of Fig. 7b obey Arrhenius law and confirm that the relaxation behavior is thermally activated in nature. From the fitting parameters, we have calculated the activation energy for both the relaxation processes as $E_\alpha = 0.134$ eV for grain and $E_\alpha = 0.202$ eV for grain boundaries driven relaxation process.

The frequency dependent ϵ' and $\tan\delta$ over the frequency range 1 Hz to 5.5 MHz for $\text{Gd}_2\text{CoMnO}_6$ at different temperatures is also presented. In Fig. 7c we observed that $\text{Gd}_2\text{CoMnO}_6$ have large ϵ' value at low frequencies and high temperatures. The dielectric spectrum is shown in Fig. 7c clearly shows the strong dispersion of dielectric permittivity at low frequencies. Further, the frequency dependent dielectric constant shows that the dispersion creeps towards the higher frequency limit when the temperature of the sample is increased. In Fig. 7d we present the frequency dependent tangent loss for nano-crystalline $\text{Gd}_2\text{CoMnO}_6$. It is evident from the figure that the $\tan\delta$ shows two regions corresponding to what is seen in Fig 7b. The same feature has been observed in the frequency dependent dielectric loss which as we have mentioned

earlier is due to the contribution of grains and grain boundaries in the relaxation process.

3.6. Impedance spectroscopy

We have calculated the real and imaginary part of impedance from permittivity data. Fig. 8 presents the detail impedance data measured for $\text{Gd}_2\text{CoMnO}_6$. Fig. 8a and 8b shows the Z' and Z'' data plotted against frequency, data is shown on logarithmic scale for clarity. Both Z' and Z'' shows similar trend with temperature evident from figures that both parameters decreases at high temperature. Z'' data is of particular interest since we can identify the peak in the to get the activation energy of relaxation process involved. In (Z'') curves there emerges a peak which reaches a maximum value at Z''_{max} corresponding to each curve, and interestingly Z''_{max} creeps to high frequency limit on increasing temperature. It is this peak shift which suggests relaxation time constant would reduce with increasing temperature. The most probable relaxation time (τ) of relaxation system can be estimated by identification the Z''_{max} in the Z'' vs $\log(f)$ plots following given relation:[48, 49]

$$\tau = \frac{1}{\omega} = \frac{1}{2\pi f} \quad (4)$$

where τ and f is the is relaxation time and frequency respectively. Relaxation behavior can further be comprehend by plotting relaxation time τ vs $10^3/T$ (K^{-1}) and analyzing its behavior with temperature. Inset of Fig. 8c shows the temperature variation of τ and it is found to follow the Arrhenius behavior given as:[48-50]

$$\tau_b = \tau_0 \exp\left(\frac{-E_a}{k_B T}\right) \quad (5)$$

where τ_0 is the pre-exponential factor, k_B the Boltzmann constant and T the absolute temperature. The data in Fig. 8c is well fitted with Eq. 5 and the activation energy (E_a) thus calculated from fitting data and its value is 0.172 eV for this material.

Fig. 8c and 8d represent Nyquist plots (Z' vs Z'') for $\text{Gd}_2\text{CoMnO}_6$. Fig. 8c-d reveal that the plot gives the combination of two semicircles in the full temperature range and the radius of the first semicircle decreases with increasing frequency. The first semicircle is due to grains and the second semicircle is due to the grain boundaries. Results from the dielectric loss and impedance spectroscopy show that the relaxation has two contributions grains and grain boundaries.

3.7. Electric conductivity

To shed some light on charge hopping and transport mechanism, AC conductivity in $\text{Gd}_2\text{CoMnO}_6$ is studied which is calculated by following relation:[51]

$$\sigma_{ac} = \epsilon_0 \omega \epsilon'' \quad (6)$$

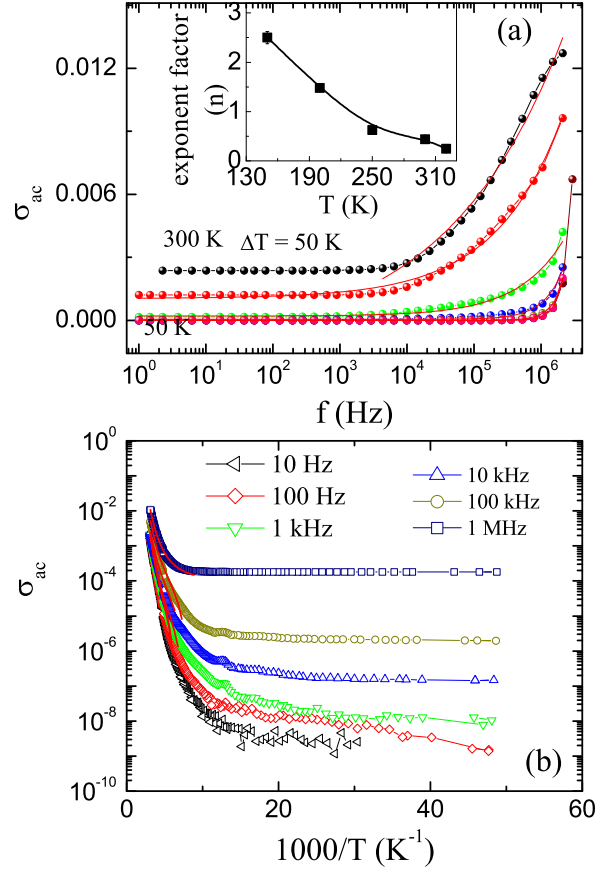


Figure 9. (Color online) (a) Presents AC conductivity (σ_{ac}) as a function of frequency. Solid red lines are fitting due to Eq. 7. Inset of Fig.(a) shows the exponent n versus the temperature for non-crystalline $\text{Gd}_2\text{CoMnO}_6$. (b) The variation of σ_{ac} with absolute temperature ($10^3/T$) is shown for $\text{Gd}_2\text{CoMnO}_6$, solid lines are fitting due to Eq. 8.

where, ϵ_0 is free space permittivity, σ_{ac} is AC conductivity, ω is angular frequency and ϵ'' is imaginary part of permittivity.

Frequency dependent AC conductivity i.e. σ_{ac} vs f measured at different temperatures is shown in Fig. 9a for $\text{Gd}_2\text{CoMnO}_6$, which reveals that at low frequencies the conductivity shows plateau region thus remains frequency independent. The dc conductivity (σ_{dc}) mainly contributes to the conductance process in this region of frequency. At higher frequencies, the conductivity does not show any plateau like behavior as seen at low frequencies, however it increases sharply with increasing frequency. Further, with increasing temperature the plateau seems to shift to higher frequency with increasing temperature. The frequency independent region gives no signature of hopping charge carriers at low frequencies. High frequency AC conductivity obey Jonscher's Universal Power Law given as:[52]

$$\sigma_{ac} = \sigma_{dc} + A\omega^n \quad (7)$$

when A is a temperature dependent constant and gives the degree of polarizability, $\omega = 2\pi f$ and $0 \leq n \leq 1$ is an temperature dependent exponent. The mobile ions and lattice interaction usually described by the value of power law exponent n .

The frequency dependent σ_{ac} is fitted with the power law in complete frequency range as shown in Fig. 9a. From the fitting parameter, n is obtained for all temperatures and plotted in the inset of Fig. 9a. It is observed that the exponent n is less than 1 at room temperature and increases with decreasing temperature which shows that the system is non-Debye's in nature.

Fig. 9b presents the σ_{ac} vs $10^3/T$ plot for Gd_2CoMn_6 selective frequencies, which shows that with increasing frequency the conductivity increases. The temperature dependent behavior of AC conductivity can be understood by fitting the data in Fig. 9b with equation below:[53–55]

$$\sigma_{ac} = \sigma_0 \exp\left(\frac{-E_a}{k_B T}\right) \quad (8)$$

where σ_0 is pre-exponent factor, k_B is Boltzmann constant and E_a is the activation energy. From the fitting parameters we have calculated that activation energy and observed that the activation energy decreases with increasing frequency. The activation energy obtained for different frequencies are given as $E_a(10 \text{ Hz}) = 3.24 \text{ eV}$, $E_a(100 \text{ Hz}) = 3.09 \text{ eV}$, $E_a(1 \text{ kHz}) = 3.00 \text{ eV}$, $E_a(10 \text{ kHz}) = 2.27 \text{ eV}$, $E_a(100 \text{ kHz}) = 2.18 \text{ eV}$ and $E_a(1 \text{ MHz}) = 2.06 \text{ eV}$

4. Conclusion

$\text{Gd}_2\text{CoMnO}_6$ nano-crystalline sample was successfully synthesis by the sol-gel method and its structural, magnetic and dielectric properties were studied. Structural study shows that the sample crystalline $P2_1/n$ space group of monoclinic structure with average crystallite size $\sim 110.9 \text{ nm}$. Magnetization study shows that the sample develops a ferromagnetic ordered state below 131 K. Further, it is found that the magnetic field greatly influences the magnetic properties and tune the phase transition. It is observed that the sample becomes almost-paramagnetic like at a high applied field of 50 kOe. Isothermal magnetization study confirms that low field sample behaves like ferromagnetic material with a finite value of the spontaneous magnetic moment. At high field limit, the spontaneous moment was not found from the Arrott plot which indicates the absence of magnetic ordering. Raman study shows the strong spin-phonon coupling present in $\text{Gd}_2\text{CoMnO}_6$. Dielectric study shows that the relaxation behavior is thermally activated process and contribution come from both grains and grain boundaries in the dielectric loss. The relaxation time is distributive in nature and thus the material is non-Debye. The impedance spectroscopy analysis and Nyquist plot study confirm that the grain and grain boundaries. The Nyquist plot deviates from ideal semicircles and further confirm the non-Debye's behavior of this material. The conductance behavior is strongly frequency dependent and the value of exponent factor n suggests that $\text{Gd}_2\text{CoMnO}_6$ is non-Debye in behavior.

Acknowledgment

We acknowledge AIRF (JNU), New Delhi India, MNIT Jaipur, India and UGC-DAE-Consortium Indore for magnetic measurement facilities, XPS measurement and Raman data respectively. We thanks Dr. A. K. Pramanik for dielectric measurement and

also acknowledge UPEA-II funding for LCR meter. Ilyas Noor Bhatti acknowledges University Grants Commission, India for financial support.

Disclosure statement

The authors declare that they have no conflict of interest.

References

- [1] N.S. Rogado, J. Li, A.W. Sleight and M.A. Subramanian, *Magnetocapacitance and Magnetoresistance Near Room Temperature in a Ferromagnetic Semiconductor: $\text{La}_2\text{NiMnO}_6$* , Adv. Mater **17**, 2225-2227 (2005).
- [2] S. Kumar, G. Giovannetti, J. van den Brink and S. Picozzi, *Theoretical prediction of multiferroicity in double perovskite Y_2NiMnO_6* , Phys. Rev. B **82**, 134429-134434 (2010).
- [3] G. Sharma, J. Saha, S.D. Kaushik, V. Siruguri and S. Patnaik, *Magnetism driven ferroelectricity above liquid nitrogen temperature in Y_2CoMnO_6* , Appl. Phys. Lett. **103** 012903-4 (2013).
- [4] A. M. Tishin and Y. I. Spichkin, *The Magnetocaloric Effect and its Application* (Taylor & Francis) (2003).
- [5] J. K. Murthy and A. Venimadhav, *Magnetodielectric behavior in $\text{La}_2\text{CoMnO}_6$ nanoparticles*, J. Appl. Phys. **111** 024102-5, (2012).
- [6] C. Hagmann and P.L. Richards, *Adiabatic demagnetization refrigerators for small laboratory experiments and space astronomy*, Cryogenics **35**, 303-309 (1995).
- [7] A. Kushino, Y. Aoki, N. Y. Yamasaki, T. Namiki, Y. Ishisaki, T. D. Matsuda, T. Ohashi, K. Mitsuda and T. Yazawa, *Erbium-doped yttrium aluminum garnet as a magnetic refrigerant for low temperature x-ray detectors*, J. Appl. Phys. **90**, 5812-5818 (2001).
- [8] J. B. Goodenough, *Theory of the Role of Covalence in the Perovskite-Type Manganites $[\text{La}, \text{M}(\text{II})]\text{MnO}_3$* , Phys. Rev. **100**, 564-573 (1955).
- [9] J. B. Goodenough and R. I. Dass, *Comment on the magnetic properties of the system $\text{Sr}_{2-x}\text{Ca}_x\text{FeMoO}_6$, $0 \leq x \leq 2$* , Int. J. Inorg. Mater. **2**, 3-4 (2000).
- [10] C. Meneghini, Sugata Ray, F. Lisio, F. Bardelli, S. Mobilio and D. D. Sarma, *Nature of Disorder in the Ordered Double Perovskite $\text{Sr}_2\text{FeMoO}_6$* , Phys. Rev. Lett. **103**, 046403-046406 (2009).
- [11] J. Snchez-Bentez, M. J. Martinez-Lope, J. A. Alonso and J. L. Garca-Muoz, *Magnetic and structural features of the $\text{NdNi}_{1-x}\text{Mn}_x\text{O}_3$ perovskite series investigated by neutron diffraction*, J. Phys.: Cond. Matter **23**(22), 226001-10 (2011).
- [12] D. C. Kakarla, K. M. Jyothinagaram, A. K. Das and V. Adyam, *Dielectric and Magnetodielectric Properties of R_2NiMnO_6 ($\text{R} = \text{Nd, Eu, Gd, Dy, and Y}$)*, Journal of the American Ceramic Society **97**(9), 2858-2866 (2014).
- [13] C. L. Bull, D. Gleeson and K. S. Knight, *Determination of B-site ordering and structural transformations in the mixed transition metal perovskites $\text{La}_2\text{CoMnO}_6$ and $\text{La}_2\text{NiMnO}_6$* , J. Phys.: Condens. Matter **15**, 49274936 (2003).
- [14] Ch. Meyer, V. Roddatis, P. Ksoll, B. Damaschke and V. Moshnyaga, *Structure, magnetism, and spin-phonon coupling in heteroepitaxial $\text{La}_2\text{CoMnO}_6/\text{Al}_2\text{O}_3(0001)$ films*, Phys Rev. B **98**, 134433-9 (2018).
- [15] W. Liu, L. Shi, S. Zhou, J. Zhao, Y. Li and Y. Guo, *Griffiths phase, spin-phonon coupling, and exchange bias effect in double perovskite $\text{Pr}_2\text{CoMnO}_6$* , J. Appl. Phys. **116**, 193901-5 (2014).
- [16] Ilyas Noor Bhatti, Imtiaz Noor Bhatti, R. N. Mahato and M. A. H. Ahsan, *Magnetic behavior, Griffiths phase and magneto-transport study in 3d based nano-crystalline double perovskite $\text{Pr}_2\text{CoMnO}_6$* , Physics Letter A **383**, 2326-2332 (2019).

- [17] Ilyas Noor Bhatti, R. N. Mahato, Imtiaz Noor Bhatti, and M. A. H. Ahsan, *Critical behavior and magnetocaloric effect in ferromagnetic nano-crystalline $\text{Pr}_2\text{CoMnO}_6$* , Physica B: Condensed Matter **558**, 59-64 (2019).
- [18] J. Blasco, J. L. Garca-Muoz, J. Garca, J. Stankiewicz, G. Subas, C. Ritter and J. A. Rodriguez-Velamazn, *Evidence of large magneto-dielectric effect coupled to a metamagnetic transition in $\text{Yb}_2\text{CoMnO}_6$* , Appl. Phys. Lett. **107**, 012902-5 (2015).
- [19] G. Sharma, J. Saha, S. D. Kaushik, V. Siruguri and S. Patnaik, *Magnetism driven ferro-electricity above liquid nitrogen temperature in Y_2CoMnO_6* , Appl. Phys. Lett. **103**, 012903-4 (2013).
- [20] A. Banerjee, J. Sannigrahi, S. Giri, and S. Majumdar, *Magnetization reversal and inverse exchange bias phenomenon in the ferrimagnetic polycrystalline compound $\text{Er}_2\text{CoMnO}_6$* , Phys. Rev. B **98**, 104414-8 (2018).
- [21] J. Y. Moon, M. K. Kim, D. G. Oh, J. H. Kim, H. J. Shin, Y. J. Choi and N. Lee, *Anisotropic magnetic properties and giant rotating magnetocaloric effect in double-perovskite, $\text{Tb}_2\text{CoMnO}_6$* , Phys. Rev. B **98**, 174424-7 (2018).
- [22] S. Yez-Vilar, E. D. Mun, V. S. Zapf, B. G. Ueland, J. S. Gardner, J. D. Thompson, J. Singleton, M. Sanchez-Andjar, J. Mira, N. Biskup, M. A. Sears-Rodriguez and C. D. Batista, *Multiferroic behavior in the double-perovskite $\text{Lu}_2\text{MnCoO}_6$* , Phys. Rev. B **84**, 134427-8 (2011).
- [23] J. Y. Moon, M. K. Kim, Y. J. Choi and N. Lee, *Giant Anisotropic Magnetocaloric Effect in Double-perovskite $\text{Gd}_2\text{CoMnO}_6$ Single Crystals*, Scientific Reports **7**, 16099-10 (2017).
- [24] X.L. Wang, J. Horvat, H.K. Liu, A.H. Li and S.X. Dou, *Spin glass state in $\text{Gd}_2\text{CoMnO}_6$ perovskite manganite*, Solid State Communications **118**, 27-30 (2001).
- [25] A. Marsh and C.C. Clark, *Metamagnetism in the perovskite compound $\text{Gd}_2\text{CoMnO}_6$* , Philosophical Magazine **19**, 449-463 (1969).
- [26] Ilyas Noor Bhatti, R. N. Mahato, Imtiaz Noor Bhatti and M. A. H. Ahsan, *Synthesis and Magnetic Study of Nano-Crystalline $\text{Gd}_2\text{CoMnO}_6$* , Materials Today: Proceedings, **17**, 216-219 (2019).
- [27] Ilyas Noor Bhatti, Imtiaz Noor Bhatti, R. N. Mahato and M. A. H. Ahsan, *Physical properties in nano-crystalline $\text{Ho}_2\text{CoMnO}_6$* , Ceramics International **46**, 46-55 (2020).
- [28] Imtiaz Noor Bhatti, R. S. Dhaka and A. K. Pramanik, *Effect of Cu^{2+} substitution in spin-orbit coupled $\text{Sr}_2\text{Ir}_{1-x}\text{Cu}_x\text{O}_4$: Structure, magnetism, and electronic properties*, Phys. Rev. B **96**, 144433-10 (2017).
- [29] Imtiaz Noor Bhatti, R. Rawat, A. Banerjee and A.K. Pramanik, *Temperature evolution of magnetic and transport behavior in 5d Mott insulator Sr_2IrO_4 : significance of magneto-structural coupling*, J. Phys.: Condens. Matter **27**, 016005-9 (2014).
- [30] Renu Gupta, Imtiaz Noor Bhatti and A. K. Pramanik, *Site dilution and charge disorder effect on physical properties in $\text{SrRu}_{1-x}\text{Ga}_x\text{O}_3$* , J. Phys.: Condens. Matter **32**, 035803-14 (2020).
- [31] X. Wang, W. Li, X. Wang, J. Zhang, L. Sun, C. Gao, J. Shang, Y. Hu and Q. Zhu, *Electrochemical properties of NiCoO_2 synthesized by hydrothermal method*, RSC Adv. **7**, 50753-50759 (2017).
- [32] B. Qiu, W. Guo, Z. Liang, W. Xia, S. Gao, Q. Wang, X. Yu, R. Zhao and R. Zou, *Fabrication of Co_3O_4 nanoparticles in thin porous carbon shells from metalorganic frameworks for enhanced electrochemical performance*, RSC Adv. **7**, 13340-13346 (2017).
- [33] H. Xia, D. Zhu, Z. Luo, Y. Yu, X. Shi, G. Yuan and J. Xie, *Hierarchically Structured $\text{Co}_3\text{O}_4@\text{Pt}@\text{MnO}_2$ Nanowire Arrays for High-Performance Supercapacitors*, Scientific Reports **3** 2978-8 (2013).
- [34] Ilyas Noor Bhatti, Imtiaz Noor Bhatti, R. N. Mahato, and M. A. H. Ahsan, *Structure, magnetic and dielectric properties in nano-crystalline $\text{Yb}_2\text{CoMnO}_6$* , Material Chemistry and Physics **244**, 122709-9 (2020).
- [35] Ilyas Noor Bhatti, Imtiaz Noor Bhatti, R. N. Mahato, and M. A. H. Ahsan, *Physical properties of nano-crystalline $\text{Sm}_2\text{CoMnO}_6$: Structure, magnetism, spin-phonon coupling and dielectric study*, Physica B: Condensed Matter **582**, 411975-10 (2020).
- [36] T. Hishida, K. Ohbayashi, and T. Saitoh, *Hidden relationship between the electrical con-*

- ductivity and the Mn 2p core-level photoemission spectra in $\text{La}_{1-x}\text{Sr}_x\text{MnO}_3$, J. Appl. Phys. **113**, 043710-6 (2013).
- [37] R. C. Sahoo, D. Paladhi and T. K. Nath, *Evidence of spin-glass like ordering and exchange bias effect in antisite-disordered nanometric $\text{La}_{1.5}\text{Ca}_{0.5}\text{CoMnO}_6$ double perovskite*, Journal of Magnetism and Magnetic Materials **436**, 77-84 (2017).
- [38] Y. Cao, W. Li, K. Xu, Y. Zhang, T. Ji, R. Zou, J. Yang, Z. Qin and J. Hu, *MnMoO₄·4H₂O nanoplates grown on a Ni foam substrate for excellent electrochemical properties*, J. Mater. Chem. A **2**, 20723-20728 (2014).
- [39] B. M. Reddy, L. Katta and G. Thrimurthulu, *Novel Nanocrystalline $\text{Ce}_{1-x}\text{La}_x\text{O}_{2\delta}$ ($x = 0.2$) Solid Solutions: Structural Characteristics and Catalytic Performance*, Chem. Mater. **22**, 467-475 (2010).
- [40] K. Wandelt and C. R. Brundle, *The interaction of oxygen with gadolinium: UPS and XPS studies*, Surf. Sci. **157**, 162-182 (1985).
- [41] M. Retuerto, A. Munoz, M.J. Martinez-Lope, J.A. Alonso, F.J. Mompén, M.T. Fernandez-Diaz and J. Sanchez-Benitez, *Magnetic Interactions in the Double Perovskites R_2NiMnO_6 ($\text{R} = \text{Tb}, \text{Ho}, \text{Er}, \text{Tm}$) Investigated by Neutron Diffraction*, Inorg. Chem. **54**(22), 10890-10900 (2015).
- [42] R. J. Booth, R. Fillman, H. Whitaker, A. Nag, M. R. Tiwari, K. V. Ramanujachary, J. Gopalakrishnan and S. E. Lofland, *An investigation of structural, magnetic and dielectric properties of R_2NiMn_6 ($\text{R} = \text{rare earth}, \text{Y}$)*, Mater. Res. Bull. **44**, 1559-1564 (2009).
- [43] M. N. Iliev, M. V. Abrashev, A. P. Litvinchuk, V. G. Hadjiev, H. Guo, and A. Gupta, *Raman spectroscopy of ordered double perovskite $\text{La}_2\text{CoMnO}_6$ thin films*, Phys. Rev. B **75** 104118-6 (2007).
- [44] C. Meyer, S. Hhn, M. Jungbauer, S. Merten, B. Damaschke, K. Samwer, and V. Moshnyaga, *Tipenhanced Raman spectroscopy (TERS) on double perovskite $\text{La}_2\text{CoMnO}_6$ thin films: field enhancement and depolarization effects*, J. Raman Spectrosc. **48** 46-52 (2017).
- [45] A. Schonhals and F. Kremer, *Broadband Dielectric Spectroscopy* Springer-Verlag Berlin Heidelberg (2003).
- [46] K. C. Kao, *Dielectric Phenomena in Solids: With Emphasis on Physical Concepts of Electronic Processes* Elsevier (2004).
- [47] Amantulla Mansuri, Ilyas Noor Bhatti, Imtiaz Noor Bhatti and Ashutosh Mishra, *Investigation of structural phase evolution and dielectric response of Co-doped BaTiO_3* , Journal of Advanced Dielectrics **08**, No. 04, 1850024-6 (2018).
- [48] S. R. Elliott, *A. C. conduction in amorphous chalcogenide and pnictide semiconductors*, Adv. Phys. **36**, 135-217 (1987).
- [49] V. K. Bhatnagar and K. L. Bhatia, *Frequency dependent electrical transport in bismuth-modified amorphous germanium sulfide semiconductors*, J. Non-Cryst. Solids **119**, 214-231 (1990).
- [50] H. A. M. Ali and M. A. Ibrahim, *Analysis of X-ray structure, dielectric properties and AC conductivity of (4E)-2-amino-3-cyanobenzo[b]oxocin-6-one*, Materials Science-Poland **34**(2), 386-392 (2016).
- [51] A. Sing, A. Gupta and R. Chatterjee, *Enhanced magnetoelectric coefficient (α) in the modified $\text{BiFeO}_3\text{PbTiO}_3$ system with large La substitution*, Appl. Phys. Lett. **93** 022902-022905 (2008).
- [52] S. Thakur, R. Rai, Igor Bdikin and M.A. Valente, *Impedance and modulus spectroscopy characterization of Tb modified $\text{Bi}_{0.8}\text{A}_{0.1}\text{Pb}_{0.1}\text{Fe}_{0.9}\text{Ti}_{0.1}\text{O}_3$ ceramics*, Mater. Res. **19** 1-8 (2016).
- [53] J. E. Kim, S. J. Kim, H. W. Choi and Y. S. Yang, *Electrical Conductivity Spectra of $4\text{BaTiO}_3\text{-SiO}_2$ Glass*, J. Korean Phys. Soc. **42**, 1224-1227 (2003).
- [54] V. S. Puli, C. Orozco, R. Picchini and C. V. Ramana, *Chemical composition-tailored $\text{Li}_x\text{Ti}_{0.1}\text{Ni}_{1-x}\text{O}$ ceramics with enhanced dielectric properties*, Materials Chemistry and Physics **184**, 82-90 (2016).
- [55] C. Chen, P. Jost, H. Volker, M. Kaminski, M. Wirtsohn, U. Engelmann, K. Kruger, F. Schlich, C. Schlockermann, R. P. S. M. Lobo and M. Wuttig, *Dielectric properties of*

amorphous phase-change materials, Phys. Rev. B **95**, 094111-9 (2017).